Structural Engineering and Mechanics, *Vol. 86*, *No. 3 (2023) 311-324*
https://doi.org/10.12989/sem.2023.86.3.311

Strain-smoothed polygonal finite elements

Hoontae Jung[1], Chaemin Lee[1,2] and Phill-Seung Lee*[1]

[1]*Department of Mechanical Engineering, Korean Advanced Institute for Science and Technology, 291 Daehak-ro, Yuseong-gu, Daejeon 34141, Republic of Korea*
[2]*Department of Safety Engineering, Chungbuk National University, Chungbuk 28644, Republic of Korea*

(*Received January 19, 2023*, *Revised March 21*, *2023*, *Accepted March 22*, *2023*)

Abstract. Herein, we present effective polygonal finite elements to which the strain-smoothed element (SSE) method is applied. Recently, the SSE method has been developed for conventional triangular and quadrilateral finite elements; furthermore, it has been shown to improve the performance of finite elements. Polygonal elements enable various applications through flexible mesh handling; however, further development is still required to use them more effectively in engineering practice. In this study, piecewise linear shape functions are adopted, the SSE method is applied through the triangulation of polygonal elements, and a smoothed strain field is constructed within the element. The strain-smoothed polygonal elements pass basic tests and show improved convergence behaviors in various numerical problems.

Keywords: finite element analysis; polygonal elements; solid elements; strain-smoothed element method

1. Introduction

The finite element method (FEM) has been widely used to analyze problems in various scientific and engineering fields (Bathe 1996, Hughes 2000, Cook 2007). The accuracy of finite element solutions relies upon the quality of the meshes used. However, because the geometries used in engineering practice are very complex, considerable effort is required to create well-shaped meshes (Jeon *et al.* 2014, Jung *et al.* 2020, Jung *et al.* 2022, Choi and Lee 2023). Conventional triangular and quadrilateral finite elements have usually been preferred owing to their efficiency and simplicity (Tabarraei and Sukumar 2006).

Recently, polygonal finite elements have been investigated as they can provide a high level of flexibility in mesh generation, transition, and refinement (Tabarraei and Sukumar 2006, Biabanaki and Khoei 2012, Biabanaki *et al.* 2014, Ho-Nguyen-Tan and Kim 2018, Khoei *et al.* 2015a, b, Talischi *et al.* 2012, Yan *et al.* 2013, Nguyen *et al.* 2020, Huang *et al.* 2017, Wachspress 1975, Floater 2003, Sukumar and Tabarraei 2004, Thomes and Menandro 2020, Natarajan *et al.* 2009, Talischi *et al.* 2014, Nguyen-Xuan 2017, Beirão da Veiga *et al.* 2013, Natarajan *et al.* 2015, Lien and Kajiya 1984); simpler meshing algorithms are possible, such as conformal decomposition (Biabanaki and Khoei 2012, Biabanaki *et al.* 2014, Ho-Nguyen-Tan and Kim 2018, Khoei *et al.* 2015a) and Voronoi tessellations (Talischi *et al.* 2012, Yan *et al.* 2013). They can effectively solve various problems such as contact problems on non-conformal meshes (Biabanaki *et al.* 2014, Khoei *et al.* 2015b), crack propagation problems with minimum remeshing (Khoei *et al.* 2015a, Nguyen *et al.* 2020), and the modeling of polycrystalline materials (Huang *et al.* 2017). Further research is required to develop polygonal finite elements that provide more accurate and reliable solutions.

Polygonal finite elements typically adopt barycentric coordinates to construct shape functions, such as Wachspress coordinates (Wachspress 1975) and mean value coordinates (Floater 2003). In these coordinates, the shape functions are constructed in the form of rational functions using the sub-areas or interior angles of an element. Then, it is difficult to accurately calculate the stiffness matrix through numerical integration. Numerous studies pertaining to the numerical integration of polygonal elements have been conducted (Tabarraei and Sukumar 2006, Sukumar and Tabarraei 2004, Thomes and Menandro 2020, Natarajan *et al.* 2009, Talischi *et al.* 2014, Nguyen-Xuan 2017). Instead, piecewise linear shape functions can be introduced such that numerical integration can be performed easily for each sub-triangle of the polygonal element (Tabarraei and Sukumar 2006, Nguyen-Xuan 2017, Jun *et al.* 2018, Kim and Lee 2018, Kim and Lee 2019).

Various strain smoothing techniques have been successfully developed for the FEM (Chen *et al.* 2001, Liu *et al.* 2007, Dai *et al.* 2007, Nguyen-Thanh *et al.* 2008, Liu *et al.* 2009a, b, Nguyen-Thoi *et al.* 2009, Nguyen-Thoi *et al.* 2011, Nguyen-Xuan *et al.* 2013, Liu *et al.* 2018, Lee and Lee 2018, Lee and Lee 2019, Lee *et al.* 2021, Lee and Park 2021). A distinct feature is that no additional degrees of freedom are required for the solution improvement. In well-known smoothed finite element methods, special smoothing domains are constructed based on a cell, node, edge, or face (Liu *et al.* 2007, Dai *et al.* 2007, Nguyen-Thanh *et al.* 2008, Liu *et al.* 2009a, b, Nguyen-Thoi *et al.* 2009, Nguyen-Thoi *et al.* 2011, Nguyen-Xuan *et al.* 2013, Liu *et al.* 2018). The recently proposed strain-smoothed element (SSE) method provides further improved solutions without requiring the construction of specific smoothing domains, unlike existing

*Corresponding author, Professor
E-mail: phillseung@kaist.edu

http://www.techno-press.com/journals/sem&subpage=7
ISSN: 1225-4568 (Print), 1598-6217 (Online)

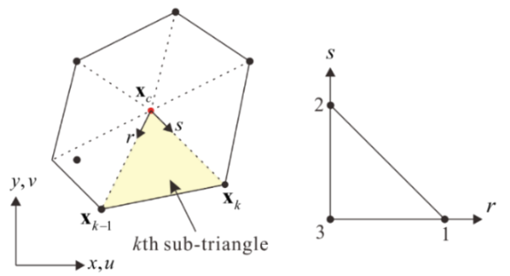

(a) (b)

Fig. 1 A polygonal element and its sub-triangles: (a) k th sub-triangle (b) Natural coordinate system for a sub-triangle

strain smoothing techniques. The SSE method has been successfully applied to 3-node triangular and 4-node quadrilateral 2D solid elements, and a 3-node MITC3+ shell element (Lee and Lee 2018, Lee and Lee 2019, Lee *et al.* 2021). Recently, a variational framework for the SSE method has been studied (Lee and Park 2021).

In this study, the SSE method is applied to polygonal finite elements to generate strain-smoothed polygonal elements. Piecewise linear shape functions are employed and strain smoothing is performed via the triangulation of polygonal elements. The polygonal elements have a smoothed strain field within the element, which is constructed by assigning smoothed strain values to the vertices of the sub-triangles. The proposed elements show further improved convergence behaviors compared with the existing polygonal elements in various numerical examples.

In the following sections, we present the formulation of the strain-smoothed polygonal elements. The performance of the proposed elements is demonstrated through basic tests and numerical examples.

2. Strain-smoothed polygonal finite elements

In this section, we present the formulation of the strain-smoothed polygonal finite elements, including the interpolations of geometry and displacement, strain smoothing, strain-displacement relation, and stiffness matrix.

2.1 Geometry and displacement interpolations

An n-sided polygonal element can be segmented into n sub-triangles based on its nodes and center point, as shown in Fig. 1(a). The position vector of the center point, $\mathbf{x}_c$, is defined using the nodal position vectors $\mathbf{x}_i$ $(i = 1, 2, \cdots, n)$ as follows

$$\mathbf{x}_c = \frac{1}{n}\sum_{i=1}^{n}\mathbf{x}_i \ \text{ with } \ \mathbf{x}_i = \begin{bmatrix} x_i & y_i \end{bmatrix}^T . \tag{1}$$

The geometry of the k th sub-triangle of the polygonal element shown in Fig. 1 can be represented by

$$\mathbf{x} = h_1\mathbf{x}_{k-1} + h_2\mathbf{x}_k + h_3\mathbf{x}_c \tag{2}$$

where $\mathbf{x}_{k-1}$ and $\mathbf{x}_k$ refer to the set of position vectors of two neighboring nodes with $\mathbf{x}_0 = \mathbf{x}_n$; $h_i(r,s)$ correspond to the shape functions of the standard isoparametric procedure for the 3-node triangular domain

$$h_1 = r\,,\ h_2 = s\,,\ h_3 = 1 - r - s\,. \tag{3}$$

Based on Eq. (2), the displacement interpolation of the k th sub-triangle of the n-sided polygonal element can be expressed as

$$\mathbf{u} = h_1\mathbf{u}_{k-1} + h_2\mathbf{u}_k + h_3\mathbf{u}_c \ \text{ with } \ \mathbf{u}_k = \begin{bmatrix} u_k & v_k \end{bmatrix}^T , \tag{4}$$

$$\mathbf{u}_c = \frac{1}{n}\sum_{i=1}^{n}\mathbf{u}_i\,, \tag{5}$$

where $\mathbf{u}_k$ is the displacement vector of node k, and $\mathbf{u}_c$ is the displacement vector of the center point of the polygonal element.

2.2 Strain smoothing

We consider the n-sided polygonal element m in a finite element mesh, as shown in Fig. 2. By adopting the standard isoparametric finite element procedure (Bathe 1996), the strain field within the k th sub-triangle of the target element m is defined as

$$\begin{aligned} &{}^{k}\boldsymbol{\varepsilon}^{(m)} = [\varepsilon_{11} \quad \varepsilon_{22} \quad 2\varepsilon_{12}]^T = {}^{k}\mathbf{B}^{(m)}\mathbf{u}^{(m)} \\ &\text{with } k = 1, 2, \cdots, n, \end{aligned} \tag{6}$$

$${}^{k}\mathbf{B}^{(m)} = \begin{bmatrix} {}^{k}\mathbf{B}_1 & {}^{k}\mathbf{B}_2 & \cdots & {}^{k}\mathbf{B}_n \end{bmatrix}, \tag{7}$$

$${}^{k}\mathbf{B}_i = \begin{bmatrix} \delta_{ik}h_{1,x} + \delta_{i(k+1)}h_{2,x} + \frac{1}{n}h_{3,x} & 0 \\ 0 & \delta_{ik}h_{1,y} + \delta_{i(k+1)}h_{2,y} + \frac{1}{n}h_{3,y} \\ \delta_{ik}h_{1,y} + \delta_{i(k+1)}h_{2,y} + \frac{1}{n}h_{3,y} & \delta_{ik}h_{1,x} + \delta_{i(k+1)}h_{2,x} + \frac{1}{n}h_{3,x} \end{bmatrix} \tag{8}$$

$$\mathbf{u}^{(m)} = \begin{bmatrix} \mathbf{u}_1 & \mathbf{u}_2 & \cdots & \mathbf{u}_n \end{bmatrix}^T \ \text{ with } \ \mathbf{u}_i = \begin{bmatrix} u_i & v_i \end{bmatrix}^T , \tag{9}$$

where ${}^{k}\mathbf{B}^{(m)}$ is the strain-displacement matrix of the k th sub-triangle, ${}^{k}\mathbf{B}_i$ is the strain-displacement matrix corresponding to node i, δ_{ik} is the Kronecker delta, $\mathbf{u}^{(m)}$ is the nodal displacement vector of the target element m, see Fig. 2(b) and Fig. 3.

The n-sided polygonal element can have a maximum of n adjacent elements through its n element edges, as shown in Fig. 2. The smoothed strain between the k th sub-triangle of the target element m and its adjacent sub-triangle of the neighboring element is calculated as follows

$$\begin{aligned} &\hat{\boldsymbol{\varepsilon}}^{(k)} = \frac{1}{A_k^{(m)} + A^{(k)}}\left(A_k^{(m)}\,{}^{k}\boldsymbol{\varepsilon}^{(m)} + A^{(k)}\boldsymbol{\varepsilon}^{(k)}\right) \\ &\text{with } k = 1, 2, \cdots, n, \end{aligned} \tag{10}$$

where ${}^{k}\boldsymbol{\varepsilon}^{(m)}$ and $A_k^{(m)}$ are the (constant) strain and area of the k th sub-triangle of the target element m, respectively; $\boldsymbol{\varepsilon}^{(k)}$ and $A^{(k)}$ are the strain and area of its neighboring sub-

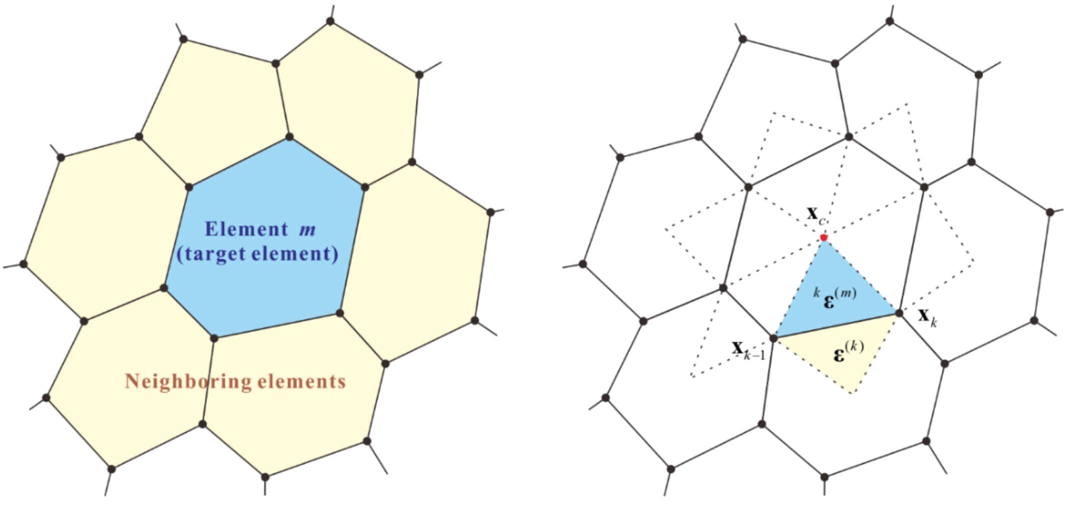

Fig. 2 A mesh of polygonal elements: (a) Target element m and its neighboring elements. (b) The strains of the k th sub-triangle of the target element and its adjacent sub-triangle in the neighboring element

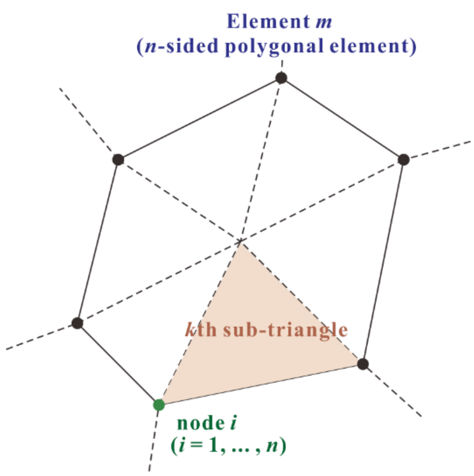

Fig. 3 Sub-triangles and nodes of an element

triangle, respectively. If no element is adjacent to the k th sub-triangle, then $\hat{\boldsymbol{\varepsilon}}^{(k)} = {}^{k}\boldsymbol{\varepsilon}^{(m)}$ is adopted (Lee and Lee 2018).

It is noteworthy that $\hat{\boldsymbol{\varepsilon}}^{(k)}$ in Eq. (10) is the smoothed strain representing the kth sub-triangle as shown in Fig. 4(a). Additionally, we can partition the polygonal element into n sub-quadrilaterals by combining the halves of two neighboring sub-triangles as shown in Fig. 4(b). Subsequently, the smoothed strain corresponding to the k th sub-quadrilateral of the target element m is defined as

$$\bar{\boldsymbol{\varepsilon}}_k = \frac{1}{A_k^{(m)} + A_{k+1}^{(m)}}\left(A_k^{(m)}\hat{\boldsymbol{\varepsilon}}^{(k)} + A_{k+1}^{(m)}\hat{\boldsymbol{\varepsilon}}^{(k+1)}\right) \quad \text{with } k = 1, 2, \cdots, n, \tag{11}$$

in which $\hat{\boldsymbol{\varepsilon}}^{(n+1)} = \hat{\boldsymbol{\varepsilon}}^{(1)}$ and $A_{n+1}^{(m)} = A_1^{(m)}$. The smoothed strain $\bar{\boldsymbol{\varepsilon}}_k$ is assigned to the center point of the kth sub-quadrilateral.

The smoothed strains for all the sub-quadrilaterals in Eq. (11) are utilized to calculate the strain at the center point of the polygonal element, as shown in Fig. 4(b)

$$\bar{\boldsymbol{\varepsilon}}_c = \frac{\sum_{k=1}^{n} A_k^{(m)}\bar{\boldsymbol{\varepsilon}}_k}{\sum_{k=1}^{n} A_k^{(m)}}. \tag{12}$$

Subsequently, we calculate the nodal strains for the sub-triangles by assigning the strains in Eq. (11) to the center point of each sub-quadrilateral, and the strain in Eq. (12) to the center point of the polygonal element, as shown in Fig. 4(c). For nodal strains $\bar{\boldsymbol{\varepsilon}}_{n1}^{(k)}$ and $\bar{\boldsymbol{\varepsilon}}_{n2}^{(k)}$ in the k th sub-triangle, the components of the nodal strains, $\bar{\varepsilon}_{n1}^{(k)}$ and $\bar{\varepsilon}_{n2}^{(k)}$, are obtained as follows:

$$\begin{bmatrix} \bar{\varepsilon}_{n1}^{(k)} \\ \bar{\varepsilon}_{n2}^{(k)} \end{bmatrix} = \begin{bmatrix} r_1 & s_1 \\ r_2 & s_2 \end{bmatrix}^{-1} \begin{bmatrix} \bar{\varepsilon}_{k-1} - \bar{\varepsilon}_c(1 - r_1 - s_1) \\ \bar{\varepsilon}_k - \bar{\varepsilon}_c(1 - r_2 - s_2) \end{bmatrix}, \tag{13}$$

where (r_1, s_1) and (r_2, s_2) are the natural coordinates of the allocated points of the smoothed strains $\bar{\boldsymbol{\varepsilon}}_{k-1}$ and $\bar{\boldsymbol{\varepsilon}}_k$, respectively (see Fig. 4(c)).

The process for obtaining the natural coordinates (r_i, s_i) in Eq. (13) is presented in Appendix A. Using the nodal strains and the strain at the center point in Eq. (12), the smoothed strain field within the element is determined via the linear interpolation for each sub-triangle. Similar to Eq. (2), the smoothed strain field within the k th sub-triangle of the element m is expressed as

$${}^{k}\bar{\boldsymbol{\varepsilon}}^{(m)} = h_1\bar{\boldsymbol{\varepsilon}}_{n1}^{(k)} + h_2\bar{\boldsymbol{\varepsilon}}_{n2}^{(k)} + h_3\bar{\boldsymbol{\varepsilon}}_c. \tag{14}$$

2.3 Strain-displacement relation and stiffness matrix

Let us consider the n-sided polygonal finite element m with n neighboring elements through its edges, as shown in Fig. 2. In the k th sub-triangle of the element m, the relation between the smoothed strain field and the nodal displacement vector is given by

$${}^{k}\bar{\boldsymbol{\varepsilon}}^{(m)} = {}^{k}\bar{\mathbf{B}}^{(m)}\bar{\mathbf{u}}^{(m)} \tag{15}$$

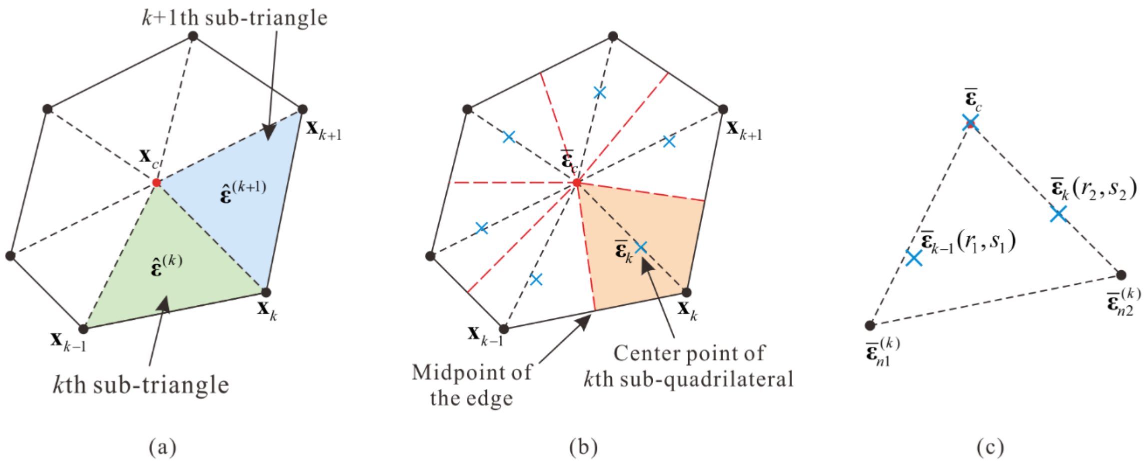

Fig. 4 Strain smoothing procedure in the strain-smoothed polygonal elements: (a) Triangulation of the polygonal element. The smoothed strain $\hat{\boldsymbol{\varepsilon}}^{(k)}$ corresponding to the kth sub-triangle. (b) Quadrangulation of the polygonal element. The smoothed strain $\bar{\boldsymbol{\varepsilon}}_k$ assigned to the center point of the kth sub-quadrilateral. (c) Calculation of the nodal strains $\bar{\boldsymbol{\varepsilon}}_{n1}^{(k)}$ and $\bar{\boldsymbol{\varepsilon}}_{n2}^{(k)}$ for the kth sub-triangle

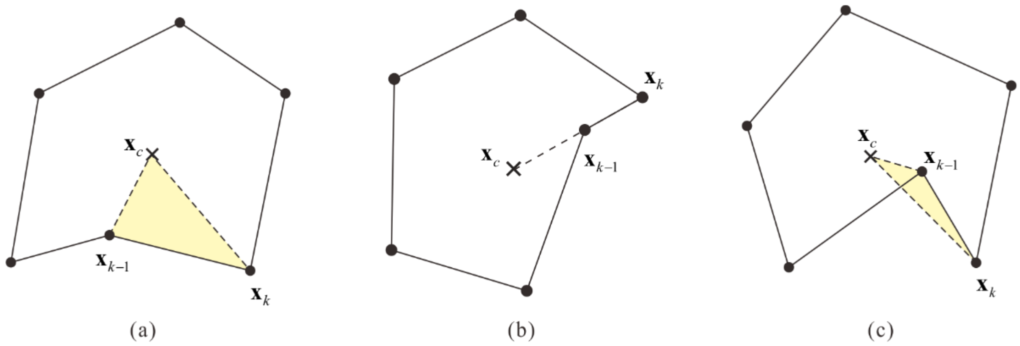

Fig. 5 Signed area of a sub-triangle when (a) $A_k^{(m)} > 0$, (b) $A_k^{(m)} = 0$, and (c) $A_k^{(m)} < 0$

with

$$ {}^{k}\bar{\mathbf{B}}^{(m)} = \begin{bmatrix} \bar{\mathbf{B}}_1 & \bar{\mathbf{B}}_2 & \cdots & \bar{\mathbf{B}}_l \end{bmatrix}, \tag{16} $$

where ${}^{k}\bar{\boldsymbol{\varepsilon}}^{(m)}$ is the smoothed strain field of the target m, ${}^{k}\bar{\mathbf{B}}^{(m)}$ is the strain-displacement matrix of the k th sub-triangle, and $\bar{\mathbf{u}}^{(m)}$ is the corresponding displacement vector.

In Eq. (16), $\bar{\mathbf{B}}_i$ $(i = 1,\ 2,\ \cdots,\ l)$ denotes the strain-displacement matrices corresponding to the node i located on the target element or neighboring elements, see Fig. 2(a). It is noteworthy that the number of components in the strain-displacement matrix and displacement vector is determined by the number of neighboring elements.

Finally, the stiffness matrix of the strain-smoothed polygonal finite element is obtained as follows

$$ \mathbf{K}^{(m)} = \sum_{k=1}^{n} {}^{k}\mathbf{K}^{(m)}, \tag{17} $$

with

$$ {}^{k}\mathbf{K}^{(m)} = \int_{{}^{k}V^{(m)}} {}^{k}\bar{\mathbf{B}}^{(m)T} \mathbf{C}^{(m)}\, {}^{k}\bar{\mathbf{B}}^{(m)} d\, {}^{k}V^{(m)}, \tag{18} $$

where ${}^{k}V^{(m)}$ is the volume of the kth sub-triangle of the element m and $\mathbf{C}^{(m)}$ is the material law matrix for the element m. To calculate the stiffness matrix, three-point Gauss integration is used for each sub-triangle domain.

Since the strain-smoothed elements have more nodes for strain calculation than standard elements, the size of the stiffness matrix of the strain-smoothed elements ($\mathbf{K}^{(m)}$) is larger than that of the standard elements. Therefore, when the strain-smoothed elements are used, the bandwidth of the corresponding global stiffness matrix becomes wider.

The proposed polygonal elements are suitable for convex and weakly concave polygonal meshes satisfying the following condition

$$ A_k^{(m)} = \frac{1}{2}(x_c y_{k-1} - x_{k-1} y_c + x_{k-1} y_k - x_k y_{k-1} + x_k y_c - x_c y_k) > 0, \tag{19} $$

where $A_k^{(m)}$ is the signed area (Lien and Kajiya 1984) of the kth sub-triangle of the target element m, and (x_i, y_i) are the coordinates of the three nodal positions of the k th sub-triangle $(i = c, k-1, k)$, as shown in Fig. 5. When the center point is located within the element and the sub-triangles of the element do not overlap each other (as shown in Fig. 5(a)), the condition is satisfied. On the other hand, the condition is not satisfied when two neighboring nodes and the center point are located in a straight line (as shown in Fig. 5(b)) or when the sub-triangles overlap each other

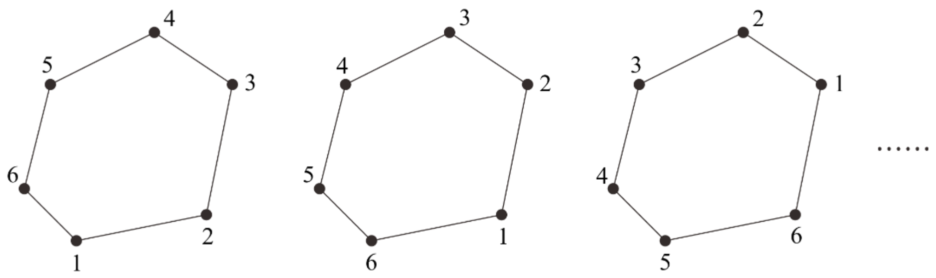

Fig. 6 Different node numbering sequences for a polygonal element

Table 1 Minimum and maximum stress values for all Gauss integration points in the patch tests (minimum stress/maximum stress)

		σ_{xx}	σ_{yy}	σ_{xy}
Normal stress (in x-direction)	Wachspress	0.99987/1.00010	-0.00004/0.00004	-0.00004/0.00009
	Mean value	0.99973/1.00030	-0.00011/0.00010	-0.00023/0.00009
	CS-FEM	1.00000/1.00000	-0.00000/0.00000	-0.00000/0.00000
	ES-FEM	1.00000/1.00000	-0.00000/0.00000	-0.00000/0.00000
	SSE (proposed)	0.99241/1.00370	-0.00183/0.00114	-0.00155/0.00190
	Reference	1.00000	0.00000	0.00000
Shear stress	Wachspress	-0.00170/0.00211	-0.00044/0.00056	0.99947/1.00050
	Mean value	-0.00425/0.00322	-0.00115/0.00092	0.99881/1.00100
	CS-FEM	-0.00000/0.00000	-0.00000/0.00000	1.00000/1.00000
	ES-FEM	-0.00000/0.00000	-0.00000/0.00000	1.00000/1.00000
	SSE (proposed)	-0.01404/0.00945	-0.00819/0.00496	0.99488/1.01180
	Reference	0.00000	0.00000	1.00000

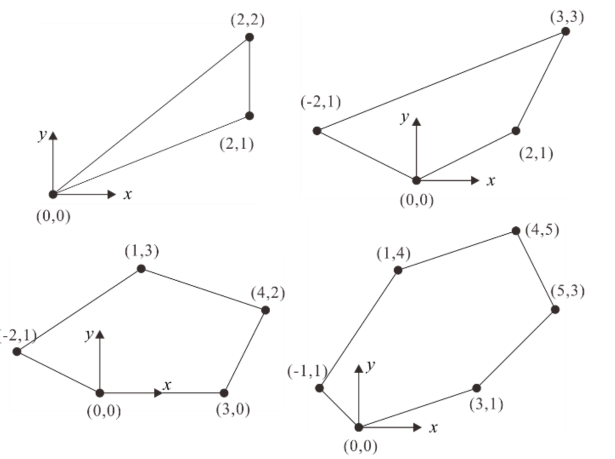

Fig. 7 Polygonal meshes used for the zero-energy mode test

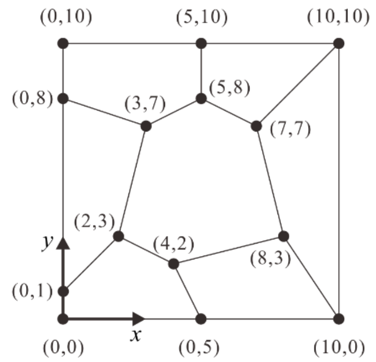

Fig. 8 A polygonal mesh used for the patch tests

(as shown in Fig. 5(c)).

3. Basic numerical tests

We conduct basic numerical tests (isotropic element, zero-energy mode, and patch tests) on the strain-smoothed polygonal elements (Bathe 1996).

To pass the isotropy test (Lee and Bathe 2004, Lee *et al.* 2012, Lee *et al.* 2014, Ko *et al.* 2016, Ko and Lee 2017, Ko *et al.* 2017a, b), the same response must be obtained for all identical elements with different node numbering sequences, as shown in Fig. 6. The proposed elements yield the same results regardless of the element node numbering sequences; hence, they pass the isotropic element test.

If no constraint exists on a single 2D solid element, then the stiffness matrix of the element must contain only three zero-energy modes corresponding to the rigid body modes (Ko *et al.* 2017a). The zero-energy mode tests are performed using the polygons from triangle to hexagon, as shown in Fig. 7. The proposed elements pass the zero-energy mode tests.

For the patch tests, the minimum number of DOFs is constrained to prevent rigid body motions, and appropriate loadings are applied to obtain a constant stress field. The same stress value should be obtained at all points on the elements to pass the patch tests. The mesh shown in Fig. 8 is used to perform the normal and shear stress patch tests, and the stress values are obtained from all Gauss integration

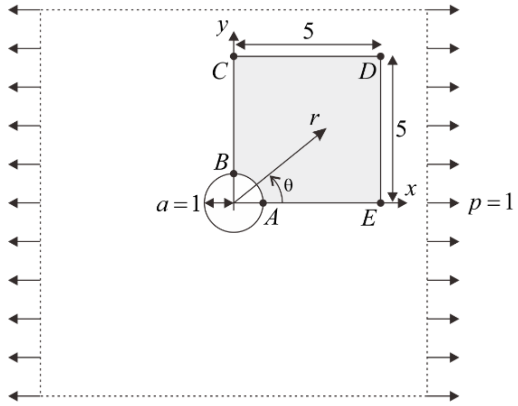

Fig. 9 Infinite plate with a circular hole ($E = 3 \times 10^7$ and $\nu = 0.3$). Only shaded domain is meshed due to symmetry

points. The proposed polygonal elements practically pass the patch tests as shown in Table 1.

4. Numerical examples

We investigate the performance of the strain-smoothed polygonal finite elements by solving the four numerical examples: an infinite plate with a circular hole, Cook's skew beam, a dam problem, and a ring problem. The unit thickness is considered for all the 2D solid problems.

The performance of the strain-smoothed polygonal finite elements (SSE) is compared with those of the polygonal finite elements based on Wachspress coordinates (Wachspress) (Wachspress 1975) and mean value coordinates (Mean value) (Floater 2003). In addition, the edge-based smoothed polygonal finite elements (ES-FEM) (Nguyen-Thoi *et al.* 2011) and the cell-based smoothed polygonal finite elements (CS-FEM) are considered for comparison. The CS-FEMs are segmented into triangular cells for strain smoothing; however, if the polygonal element is a quadrilateral, then this element is segmented into four quadrilateral cells (Liu *et al.* 2007, Dai *et al.* 2007).

The convergence of the elements is evaluated through their displacements at specific locations and stress distributions. Reference solutions are obtained using sufficiently fine meshes of 9-node quadrilateral finite elements.

The relative error in strain energy E_r is measured as follows

$$E_r = \frac{|E_{\text{ref}} - E_h|}{E_{\text{ref}}}, \tag{20}$$

where E_{ref} is the reference strain energy and E_h is the strain energy calculated from the finite element solutions. The optimal convergence behavior for linear elements is expressed as

$$E_r \cong ch^2, \tag{21}$$

where c is a constant and h is the element size (Bathe 1996).

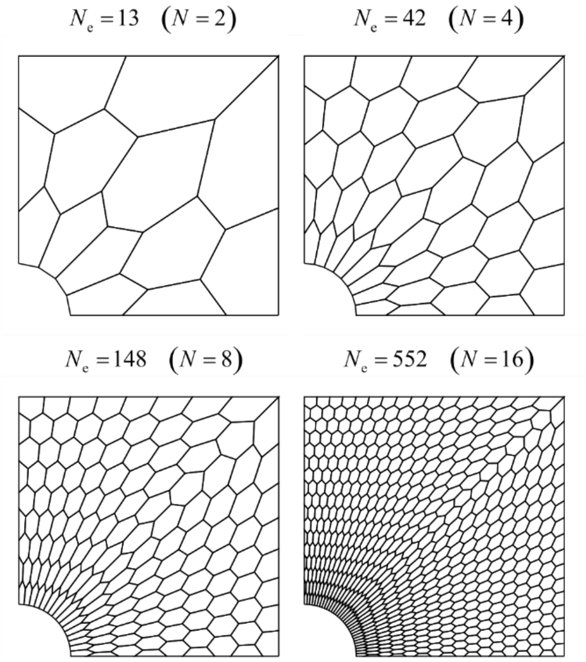

Fig. 10 Polygonal meshes used for the infinite plate with a circular hole

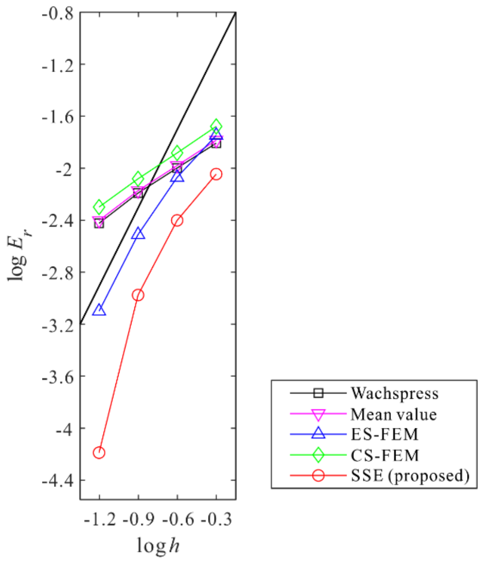

Fig. 11 Convergence curves for Cook's skew beam. The bold line represents the optimal convergence rate

4.1 Infinite plate with a circular hole

We solve the problem of infinite plate with a circular hole shown in Fig. 9 (Liu *et al.* 2007, Lee and Lee 2018).

The radius of the circular hole is $a = 1$, and the infinite plate is subjected to a far-field traction $p = 1$ (force per area) in the x-direction. The plane strain condition is considered with Young's modulus $E = 3 \times 10^7$ and Poisson's ratio $\nu = 0.3$. Owing to symmetry, one-quarter of the plate is modeled as shown in Fig. 9, and the corresponding boundary conditions are imposed as follows: $u = 0$ along BC and $v = 0$ along AE. Fig. 10 shows meshes used with the total numbers of elements N_e =13,

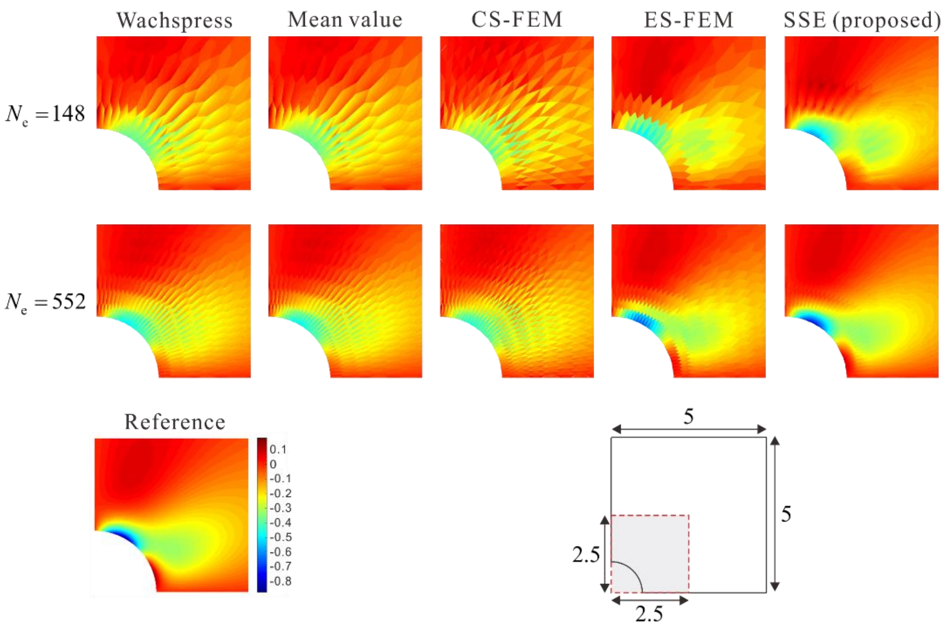

Fig. 12 Stress distributions (σ_{xy}) for the infinite plate with a circular hole. Only 2.5×2.5 area around the hole is plotted. The reference stress distribution is obtained using an 8,192 element mesh of 9-node quadrilateral elements

Table 2 Relative errors in the horizontal displacement ($|u_{\text{ref}} - u_h|/|u_{\text{ref}}| \times 100$) at point A in the infinite plate with a circular hole

N_e	Wachspress	Mean value	CS-FEM	ES-FEM	SSE (proposed)
13	12.831	13.566	19.302	16.419	6.324
42	8.666	9.023	11.862	7.517	2.898
148	5.694	5.913	7.442	2.604	0.729
552	3.317	3.479	4.459	0.631	0.022

Reference solution: $u_{\text{ref}} = 9.101 \times 10^{-8}$

Table 3 Relative errors in the vertical displacement ($|v_{\text{ref}} - v_h|/|v_{\text{ref}}| \times 100$) at point B in the infinite plate with a circular hole

N_e	Wachspress	Mean value	CS-FEM	ES-FEM	SSE (proposed)
13	19.143	19.304	21.998	16.798	14.139
42	16.809	17.156	19.225	10.158	8.187
148	13.117	13.530	15.748	4.200	2.641
552	8.387	8.785	10.896	1.029	0.428

Reference solution: $v_{\text{ref}} = -3.034 \times 10^{-8}$

42, 148 and 552 (or the numbers of elements along the upper edge N =2, 4, 8 and 16, respectively). The element size h is defined as $h = 1/N$.

The traction boundary conditions are imposed along CD and DE using the following analytical solutions (Timoshenko 1970)

$$\sigma_{xx}(r,\theta) = p\left(1 - \frac{a^2}{r^2}\left(\frac{3}{2}\cos 2\theta + \cos 4\theta\right) + \frac{3a^4}{2r^4}\cos 4\theta\right), \quad (22)$$

$$\sigma_{yy}(r,\theta) = p\left(-\frac{a^2}{r^2}\left(\frac{1}{2}\cos 2\theta - \cos 4\theta\right) - \frac{3a^4}{2r^4}\cos 4\theta\right), \quad (23)$$

$$\sigma_{xy}(r,\theta) = p\left(-\frac{a^2}{r^2}\left(\frac{1}{2}\sin 2\theta + \sin 4\theta\right) + \frac{3a^4}{2r^4}\sin 4\theta\right), \quad (24)$$

where r and θ are the distance from the origin ($x = y = 0$) and counterclockwise angle from the positive x-axis, respectively.

The convergence curves obtained using E_r in Eq. (20) are shown in Fig. 11. The relative errors in the horizontal displacement at point A and the vertical displacement at point B are listed in Tables 2-3, respectively. The distributions of the calculated stress component σ_{xy} for the 2.5×2.5 area around the hole are shown in Fig. 12. The reference solutions are obtained using an 8,192 element mesh of 9-node quadrilateral elements. The proposed elements provide improved convergence behaviors compared with the elements based on Wachspress coordinates and mean value coordinates, the cell-based smoothed elements, and the edge-based smoothed elements.

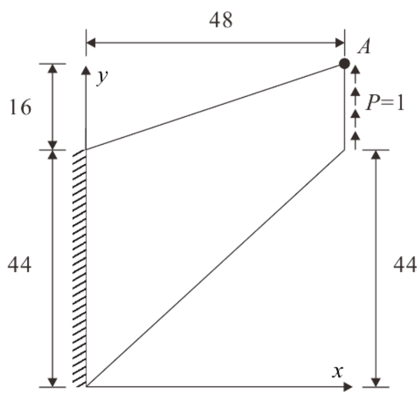

Fig. 13 Cook's skew beam ($E = 3 \times 10^7$ and $\nu = 0.3$)

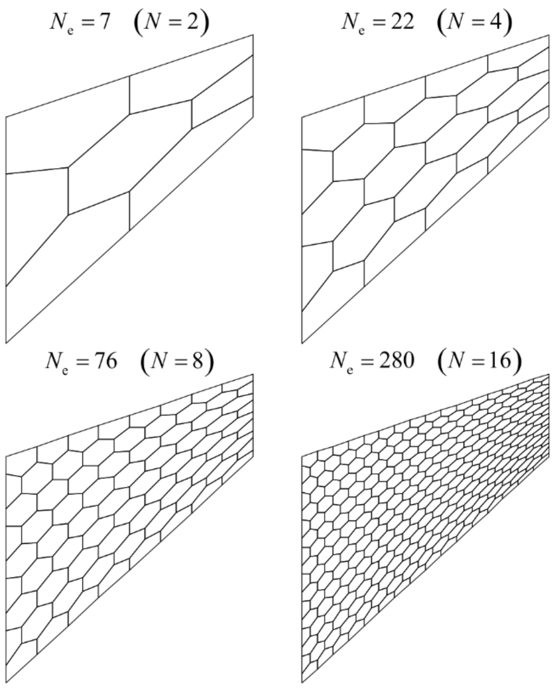

Fig. 14 Polygonal meshes used for Cook's skew beam

4.2 Cook's skew beam

The well-known Cook's skew beam problem is solved, as shown in Fig. 13 (Cook 2007). The left side of the structure is clamped, and a distributed shearing force of total magnitude $P = 1$ is exerted on the right edge. The plane stress condition is assumed with Young's modulus $E = 3 \times 10^7$ and Poisson's ratio $\nu = 0.3$. Solutions are obtained for meshes with the total numbers of elements N_e =7, 22, 76 and 280 (or the numbers of elements along the upper edge N =2, 4, 8 and 16, respectively), as shown in Fig. 14. The element size h is defined by $h = 1/N$.

The convergence curves for E_r in Eq. (20) are depicted in Fig. 15. The convergences in the normalized horizontal displacement at point A are shown in Fig. 16. The relative errors in the horizontal displacement at point A are listed in Table 4. The reference solutions are obtained using a 64×64 mesh of 9-node quadrilateral elements. Among the polygonal elements considered, the proposed elements provide the best solution accuracy.

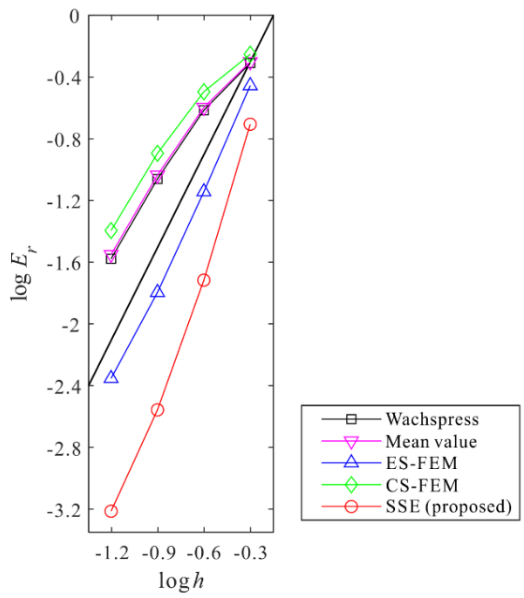

Fig. 15 Convergence curves for Cook's skew beam. The bold line represents the optimal convergence rate

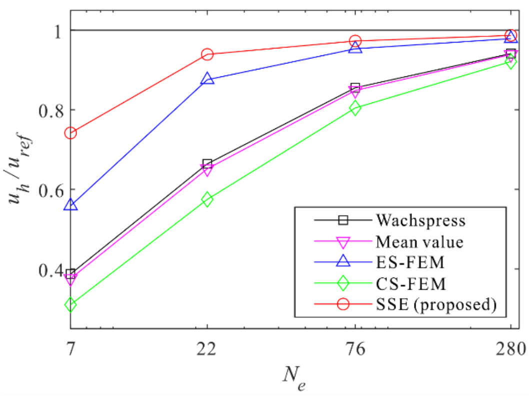

Fig. 16 Normalized horizontal displacements (u_h/u_{ref}) at point A in Cook's skew beam

The computational efficiency of the considered elements is compared in Fig. 17. We plot the relations between computation times versus the errors in strain energy. The solutions are obtained using the meshes where the numbers of elements along the upper edge N = 8, 16, 32, 64 and 128. In addition, a standard 3-node triangular element (named T3) is employed with meshes obtained by triangulation of polygons as shown in Fig. 18, and the computational efficiency of the T3 element is presented in Fig. 17. Computations are conducted using a personal computer with Intel Core i7-4790, 3.60 GHz CPU, and 8 GB RAM. The skyline solver is used to solve a linear system of equations. As shown in Fig. 17, the proposed elements give more accurate solutions compared with other elements at similar computation time levels. In other words, the proposed elements exhibit the best computational efficiency among the elements considered in this problem.

4.3 Dam problem

A 2D dam structure is subjected to the following surface

Table 4 Relative errors in the horizontal displacement ($|u_{\text{ref}} - u_h|/|u_{\text{ref}}| \times 100$) at point A in Cook's skew beam problem

N_e	Wachspress	Mean value	CS-FEM	ES-FEM	SSE (proposed)
7	61.270	62.422	68.968	44.119	25.828
22	33.579	34.823	42.504	12.452	6.089
76	14.478	15.140	19.537	4.681	2.710
280	5.879	6.136	7.879	2.127	1.301

Reference solution: u_{ref} = -6.301 × 10^{-7}

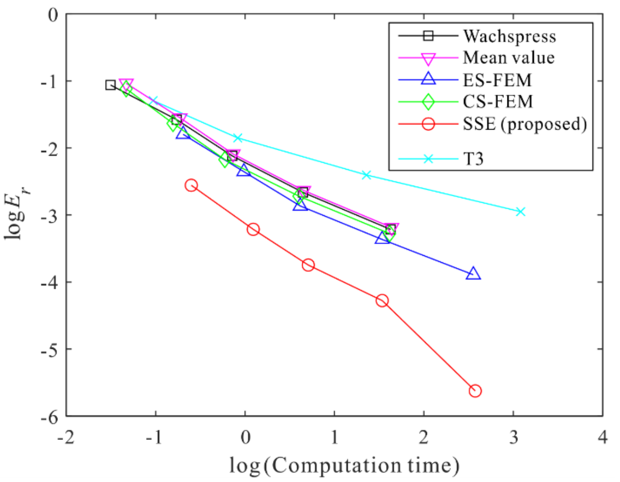

Fig. 17 Computational efficiency curves for Cook's skew beam. The computation times are measured in seconds

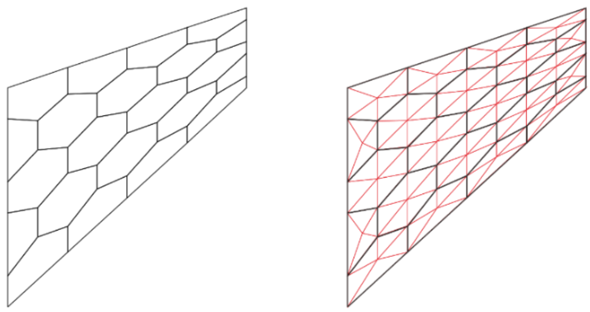

(a) (b)

Fig. 18 Mesh obtained by triangulation of polygons (N = 4): (a) Polygonal mesh (92 DOFs). (b) Triangular mesh (136 DOFs)

force (force per length) on its left edge, as shown in Fig. 19 (Lee *et al.* 2021)

$$f_s = \begin{cases} 5-y & 0 \le y \le 5 \\ (y-5)^{1/5} & 5 \le y \le 10 \end{cases}. \tag{25}$$

The clamped boundary condition is applied along the bottom edge. The plane strain condition is employed with Young's modulus $E = 3 \times 10^{10}$ and Poisson's ratio $\nu = 0.2$. We use meshes with the total numbers of elements N_e =13, 42, 148 and 552, as shown in Fig. 20. The element size h is $h = 1/N$, where N is the number of elements along the left edge.

The convergence curves are obtained using E_r in Eq. (20), as shown in Fig. 21. The reference solutions are

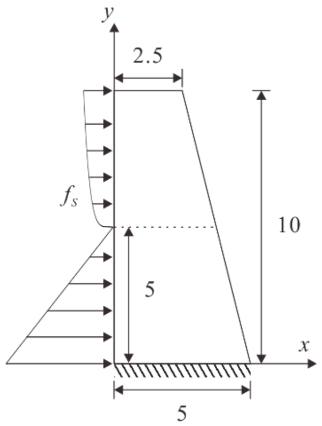

Fig. 19 Dam problem ($E = 3 \times 10^{10}$ and $\nu = 0.2$)

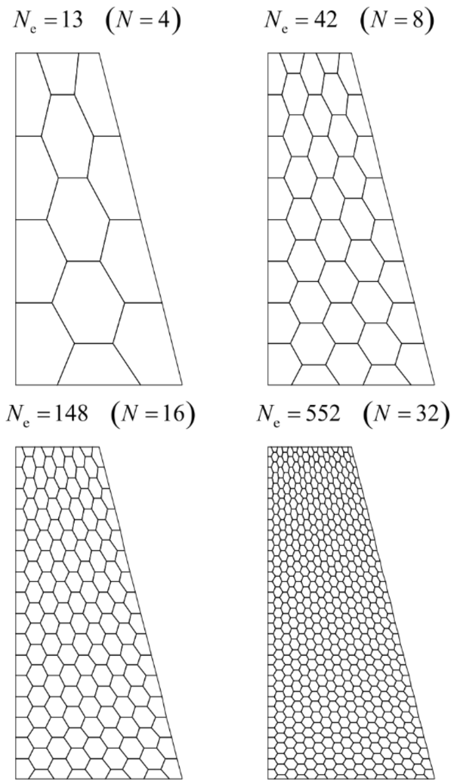

Fig. 20 Polygonal meshes used for the dam problem

obtained using a 64 × 128 mesh of 9-node quadrilateral elements. The proposed elements demonstrate significantly improved convergence behaviors compared with the elements based on Wachspress coordinates and mean value coordinates, the cell-based smoothed elements, and the edge-based smoothed elements.

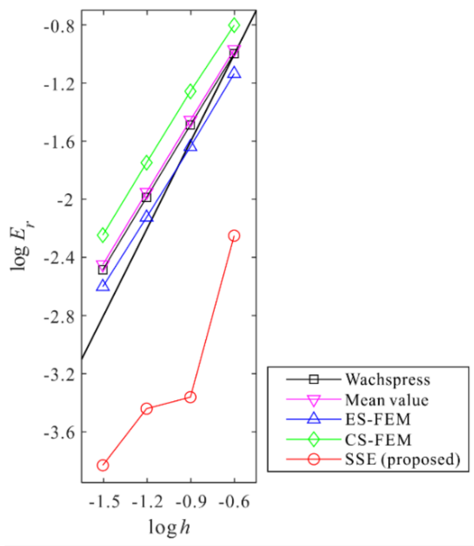

Fig. 21 Convergence curves for the dam problem. The bold line represents the optimal convergence rate

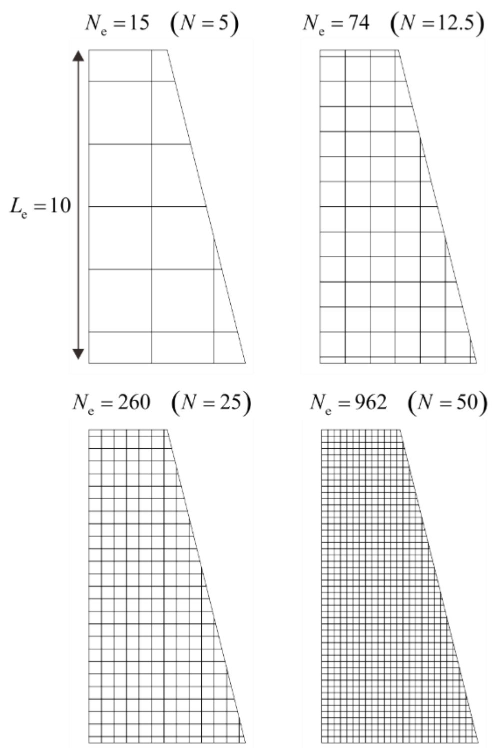

Fig. 22 Polygonal meshes constructed using the paving and cutting algorithm for the dam problem

In addition, we evaluate the performance of the proposed elements for meshes constructed using the paving and cutting algorithm. Using the meshing algorithm, the interior of the problem domain is uniformly meshed for quadrilateral elements, but the boundary is meshed for polygonal elements (Biabanaki and Khoei 2012, Biabanaki *et al.* 2014, Ho-Nguyen-Tan and Kim 2018, Khoei *et al.* 2015a). Fig. 22 shows the resulting meshes obtained by using the meshing algorithm for this problem. The uniform grid sizes used are $h_{\text{grid}} = 2$, 0.8, 0.4, and 0.2. For convergence studies, the element size h is defined as $h = 1/N$, with an equivalent number of elements $N = L_e/h_{\text{grid}}$ (characteristic length $L_e = 10$ in this problem). Fig. 23 shows the convergence curves obtained using E_r in Eq. (20). The proposed elements provide improved solution accuracy, even when used with the paving and cutting algorithm.

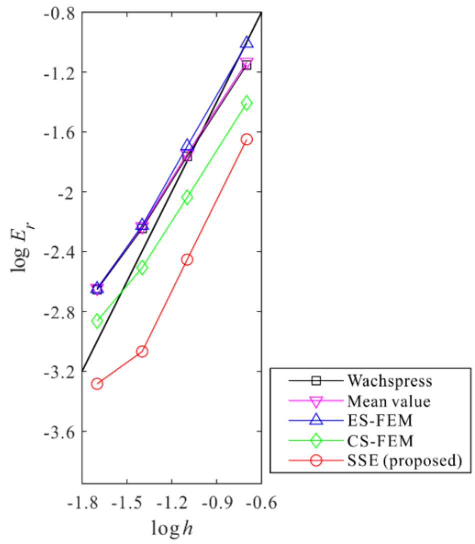

Fig. 23 Convergence curves for the dam problem when the meshes with the paving and cutting algorithm are utilized. The bold line represents the optimal convergence rate

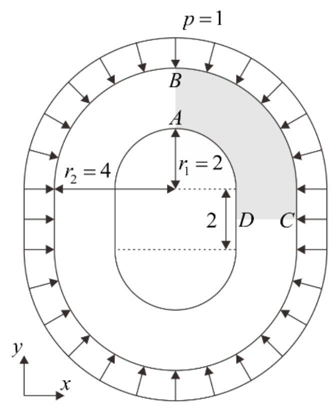

Fig. 24 Ring problem ($E = 3 \times 10^3$ and $\nu = 0.3$). Only shaded domain is considered for analysis owing to symmetry

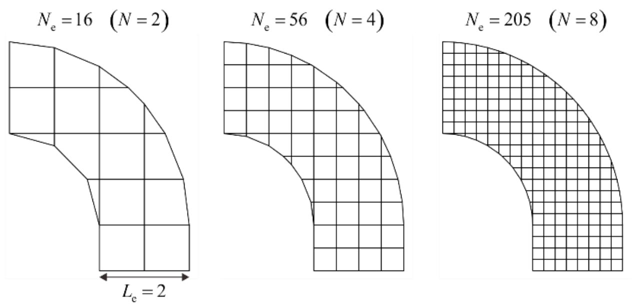

Fig. 25 Polygonal meshes constructed using the paving and cutting algorithm for the ring problem

Table 5 Relative errors in the vertical displacement ($|v_{\rm ref} - v_h|/|v_{\rm ref}| \times 100$) at point A in the ring problem

N_e	Wachspress	Mean value	CS-FEM	ES-FEM	SSE (proposed)
16	99.953	101.652	74.198	79.101	8.186
56	31.261	32.001	22.724	23.946	2.754
205	8.337	8.549	5.687	5.568	0.447

Reference solution: $v_{\rm ref} = 5.996 \times 10^{-4}$

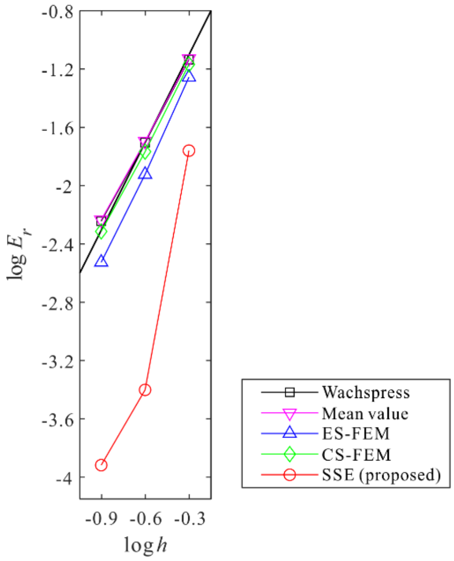

Fig. 26 Convergence curves for the ring problem. The bold line represents the optimal convergence rate

4.4 Ring problem

A 2D ring structure is subjected to a surface force (force per length) in the direction normal to the surface as shown in Fig. 24. For this symmetric problem, one quarter of the ring is considered with the following boundary conditions: $u = 0$ along AB, and $v = 0$ along CD, as shown in Fig. 24. The plane stress condition is assumed with Young's modulus $E = 3 \times 10^3$ and Poisson's ratio $\nu = 0.3$.

As shown in Fig. 25, meshes with the total numbers of elements N_e =16, 56 and 205 are obtained by using the paving and cutting algorithm. Here, the uniform grid sizes are $h_{\rm grid}$ =1/2, 1/4, and 1/8 of the ring width L_e= 2. The element size h is defined as $h = 1/N$, with an equivalent number of elements $N = L_e/h_{\rm grid}$.

The convergence curves for E_r in Eq. (20) are shown in Fig. 26. The von Mises stress distributions are shown in Fig. 27. The convergences in the normalized vertical displacement at point A are shown in Fig. 28. The relative errors in the vertical displacement at point A are listed in Table 5. The reference solutions are obtained using a 64×64 mesh of 9-node quadrilateral elements. The proposed elements demonstrate significantly better convergence behaviors than the other elements considered.

In all the numerical examples presented, the proposed elements consistently yield better convergence behaviors compared with the elements using Wachspress shape functions, the cell-based smoothed elements, and the edge-based smoothed elements. Additionally, the proposed elements are effective when used with the paving and cutting algorithm.

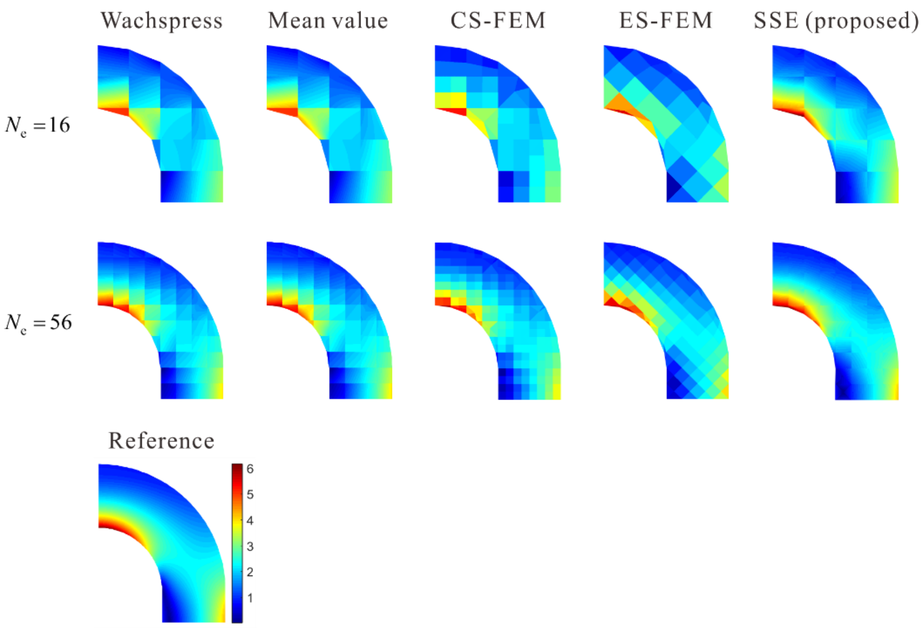

Fig. 27 von Mises stress distributions for the ring problem. The reference stress distribution is obtained using a 64×64 mesh of 9-node quadrilateral elements

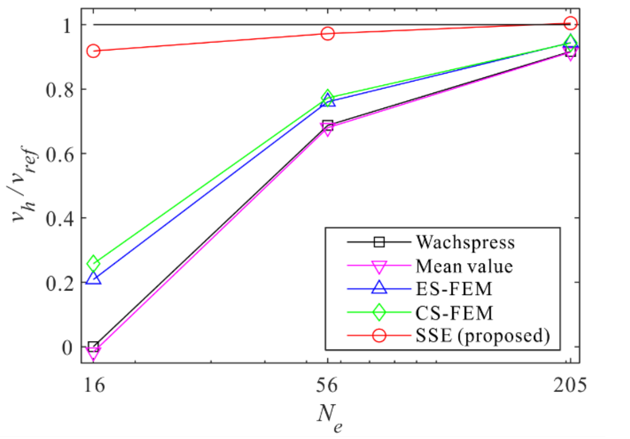

Fig. 28 Normalized vertical displacements (v_h/v_{ref}) at point A in the ring problem

5. Conclusions

In this study, we proposed the strain-smoothed polygonal finite elements. Instead of using complex shape functions for polygonal elements, piecewise linear shape functions were employed to triangulate the elements for strain smoothing. We first calculated the smoothed strains for the elements using all the strains of all neighboring elements. Subsequently, smoothed strains were assigned to the vertices of the sub-triangles of the elements, which resulted in a piecewise linear strain field for the strain-smoothed polygonal elements.

The strain-smoothed polygonal elements passed the basic tests (i.e., isotropic element, zero-energy mode, and patch tests). In addition, the elements showed improved convergence behaviors compared with previously developed elements in various numerical examples. The strain-smoothed polygonal elements can be effectively used in various applications, such as contact problems on non-conformal meshes (Biabanaki *et al.* 2014, Khoei *et al.* 2015b) and crack analysis with minimal remeshing (Khoei *et al.* 2015a, Nguyen *et al.* 2020).

Acknowledgments

This work was supported by the Nuclear Safety Research Program through the Korea Foundation Of Nuclear Safety (KoFONS) using the financial resource granted by the Nuclear Safety and Security Commission (NSSC) of the Republic of Korea (No. 2106045).

References

Bathe, K.J. (1996), *Finite Element Procedures*, Prentice Hall, New
Beirão da Veiga, L., Brezzi, F. and Marini, L.D. (2013), "Virtual elements for linear elasticity problems", *SIAM J. Numer. Anal.*, **51**(2), 794-812. https://doi.org/10.1137/120874746.
Biabanaki, S.O.R. and Khoei, A.R. (2012), "A polygonal finite element method for modeling arbitrary interfaces in large deformation problems", *Comput. Mech.*, **50**, 19-33. https://doi.org/10.1007/s00466-011-0668-4.
Biabanaki, S.O.R., Khoei, A.R. and Wriggers, P. (2014), "Polygonal finite element methods for contact-impact problems on non-conformal meshes", *Comput. Meth. Appl. Mech. Eng.*, **269**, 198-221. https://doi.org/10.1016/j.cma.2013.10.025.
Chen, J.S., Wu, C.T., Yoon, S. and You, Y. (2001), "Stabilized conforming nodal integration for Galerkin mesh-free methods", *Int. J. Numer. Meth. Eng.*, **50**, 435-466. https://doi.org/10.1002/1097-0207(20010120)50:2<435::AID-NME32>3.0.CO;2-A.
Choi, H.G. and Lee, P.S. (2023), "Towards improving the 2D-MITC4 element for analysis of plane stress and strain problems", *Comput. Struct.*, **275**, 106933. https://doi.org/10.1016/j.compstruc.2022.106933.
Cook, R.D. (2007), *Concepts and Applications of Finite Element Analysis*, John Wiley & Sons, New York.
Dai, K.Y., Liu, G.R. and Nguyen, T.T. (2007), "An n-sided polygonal smoothed finite element method (nSFEM) for solid mechanics", *Finite Elem. Anal. Des.*, **43**, 847-860. https://doi.org/10.1016/j.finel.2007.05.009.
Floater, M.S. (2003), "Mean value coordinates", *Comput. Aid. Geom. Des.*, **20**, 19-27. https://doi.org/10.1016/S0167-8396(03)00002-5.
Ho-Nguyen-Tan, T. and Kim, H.G. (2018), "A new strategy for finite-element analysis of shell structures using trimmed quadrilateral shell meshes: A paving and cutting algorithm and a pentagonal shell element", *Int. J. Numer. Meth. Eng.*, **114**, 1-27. https://doi.org/10.1002/nme.5730.
Huang, X., Ding, W., Zhu, Y. and Yang, C. (2017), "Crack propagation simulation of polycrystalline cubic boron nitride abrasive materials based on cohesive element method", *Comput. Mater. Sci.*, **138**, 302-314. https://doi.org/10.1016/j.commatsci.2017.07.007.
Hughes, T.J.R. (2000), *The Finite Element Method: Linear Static and Dynamic Finite Element Analysis*, Dover Publications, Mineola, New York.
Jeon, H.M., Lee, P.S. and Bathe, K.J. (2014), "The MITC3 shell finite element enriched by interpolation covers", *Comput. Struct.*, **134**, 128-142. https://doi.org/10.1016/j.compstruc.2013.12.003.
Jun, H., Yoon, K., Lee, P.S. and Bathe, K.J. (2018), "The MITC3+ shell element enriched in membrane displacements by interpolation covers", *Comput. Meth. Appl. Mech. Eng.*, **337**, 458-480. https://doi.org/10.1016/j.cma.2018.04.007.
Jung, J., Jun, H. and Lee, P.S. (2022), "Self-updated four-node finite element using deep learning", *Comput. Mech.*, **69**, 23-44. https://doi.org/10.1007/s00466-021-02081-7.
Jung, J., Yoon, K. and Lee, P.S. (2020), "Deep learned finite elements", *Comput. Meth. Appl. Mech. Eng.*, **372**, 113401. https://doi.org/10.1016/j.cma.2020.113401.
Khoei, A.R., Yasbolaghi, R. and Biabanaki, S.O.R (2015a), "A polygonal finite element method for modeling crack propagation with minimum remeshing", *Int. J. Fract.*, **194**, 123-148. https://doi.org/10.1007/s10704-015-0044-z.
Khoei, A.R., Yasbolaghi, R. and Biabanaki, S.O.R (2015b), "A polygonal-FEM technique in modeling large sliding contact on non-conformal meshes: A study on polygonal shape functions", *Eng. Comput.*, **32**(5), 1391-1431. https://doi.org/10.1108/EC-04-2014-0070.
Kim, S. and Lee, P.S. (2018), "A new enriched 4-node 2D solid finite element free from the linear dependence problem", *Comput. Struct.*, **202**, 25-43. https://doi.org/10.1016/j.compstruc.2018.03.001.
Kim, S. and Lee, P.S. (2019), "New enriched 3D solid finite elements: 8-node hexahedral, 6-node prismatic, and 5-node pyramidal elements", *Comput. Struct.*, **216**, 40-63. https://doi.org/10.1016/j.compstruc.2018.12.002.
Ko, Y. and Lee, P.S. (2017), "A 6-node triangular solid-shell element for linear and nonlinear analysis", *Int. J. Numer. Meth.*

Eng., **111**(13), 1203-1230. https://doi.org/10.1002/nme.5498.

Ko, Y., Lee, P.S. and Bathe K.J. (2016), "The MITC4+ shell element and its performance", *Comput. Struct.*, **169**, 57-68. https://doi.org/10.1016/j.compstruc.2016.03.002.

Ko, Y., Lee, P.S. and Bathe K.J. (2017a), "A new MITC4+ shell element", *Comput. Struct.*, **182**, 404-418. https://doi.org/10.1016/j.compstruc.2016.11.004.

Ko, Y., Lee, P.S. and Bathe K.J. (2017b), "A new 4-node MITC element for analysis of two-dimensional solids and its formulation in a shell element", *Comput. Struct.*, **192**, 34-49. https://doi.org/10.1016/j.compstruc.2017.07.003.

Lee, C. and Lee, P.S. (2018), "A new strain smoothing method for triangular and tetrahedral finite elements", *Comput. Meth. Appl. Mech. Eng.*, **341**, 939-955. https://doi.org/10.1016/j.cma.2018.07.022.

Lee, C. and Lee, P.S. (2019), "The strain-smoothed MITC3+ shell finite element", *Comput. Struct.*, **223**, 106096. https://doi.org/10.1016/j.compstruc.2019.07.005.

Lee, C. and Park, J. (2021), "A variational framework for the strain-smoothed element method", *Comput. Math. Appl.*, **94**, 76-93. https://doi.org/10.1016/j.camwa.2021.04.025.

Lee, C., Kim, S. and Lee, P.S. (2021), "The strain-smoothed 4-node quadrilateral finite element", *Comput. Meth. Appl. Mech. Eng.*, **373**, 113481. https://doi.org/10.1016/j.cma.2020.113481.

Lee, P.S. and Bathe, K.J. (2004), "Development of MITC isotropic triangular shell finite elements", *Comput. Struct.*, **82**(11-12), 945-962. https://doi.org/10.1016/j.compstruc.2004.02.004.

Lee, Y., Lee, P.S. and Bathe, K.J. (2014), "The MITC3+ shell element and its performance", *Comput. Struct.*, **138**, 12-23. https://doi.org/10.1016/j.compstruc.2014.02.005.

Lee, Y., Yoon, K. and Lee, P.S. (2012), "Improving the MITC3 shell finite element by using the Hellinger-Reissner principle", *Comput. Struct.*, **110-111**, 93-106. https://doi.org/10.1016/j.compstruc.2012.07.004.

Lien, S. and Kajiya, J.T. (1984), "A symbolic method for calculating the integral properties of arbitrary nonconvex polyhedral", *IEEE Comput. Graph. Appl.*, **4**(10), 35-42. https://doi.org/10.1109/MCG.1984.6429334.

Liu, F., Yu, C. and Yang, Y. (2018), "An edge-based smoothed numerical manifold method and its application to static, free and forced vibration analyses", *Eng. Anal. Bound. Elem.*, **86**, 19-30. https://doi.org/10.1016/j.enganabound.2017.10.006.

Liu, G.R., Dai, K.Y. and Nguyen, T.T. (2007), "A smoothed finite element method for mechanics problems", *Comput. Mech.*, **39**, 859-877. https://doi.org/10.1007/s00466-006-0075-4.

Liu, G.R., Nguyen-Thoi, T. and Lam, K.Y. (2009b), "An edge-based smoothed finite element method (ES-FEM) for static, free and forced vibration analyses of solids", *J. Sound Vib.*, **320**, 1100-1130. https://doi.org/10.1016/j.jsv.2008.08.027.

Liu, G.R., Nguyen-Thoi, T., Nguyen-Xuan, H. and Lam, K.Y. (2009a), "A node-based smoothed finite element method (NS-FEM) for upper bound solutions to solid mechanics problems", *Comput. Struct.*, **87**, 14-26. https://doi.org/10.1016/j.compstruc.2008.09.003.

Natarajan, S., Bordas, S.P.A. and Ooi, E.T. (2015), "Virtual and smoothed finite elements: A connection and its application to polygonal/polyhedral finite element methods", *Int. J. Numer. Meth. Eng.*, **104**(13), 1173-1199. https://doi.org/10.1002/nme.4965.

Natarajan, S., Bordas, S.P.A. and Roy Mahapatra, D. (2009), "Numerical integration over arbitrary polygonal domains based on Schwarz-Christoffel conformal mapping", *Int. J. Numer. Meth. Eng.*, **80**, 103-134. https://doi.org/10.1002/nme.2589.

Nguyen, N.V., Lee, D., Nguyen-Xuan, H. and Lee, J. (2020), "A polygonal finite element approach for fatigue crack growth analysis of interfacial cracks", *Theor. Appl. Fract. Mech.*, **108**, 102576. https://doi.org/10.1016/j.tafmec.2020.102576.

Nguyen-Thanh, N., Rabczuk, T., Nguyen-Xuan, H. and Bordas, S.P.A. (2008), "A smoothed finite element method for shell analysis", *Comput. Meth. Appl. Mech. Eng.*, **198**, 165-177. https://doi.org/10.1016/j.cma.2008.05.029.

Nguyen-Thoi, T., Liu, G.R. and Nguyen-Xuan, H. (2011), "An n-sided polygonal edge-based smoothed finite element method (nES-FEM) for solid mechanics", *Int. J. Numer. Meth. Biomed. Eng.*, **27**, 1446-1472. https://doi.org/10.1002/cnm.1375.

Nguyen-Thoi, T., Liu, G.R., Lam, K.Y. and Zhang, G.Y. (2009), "A face-based smoothed finite element method (FS-FEM) for 3D linear and geometrically non-linear solid mechanics problems using 4-node tetrahedral elements", *Int. J. Numer. Meth. Eng.*, **78**, 324-353. https://doi.org/10.1002/nme.2491.

Nguyen-Xuan, H. (2017), "A polygonal finite element method for plate analysis", *Comput. Struct.*, **188**, 45-62. https://doi.org/10.1016/j.compstruc.2017.04.002.

Nguyen-Xuan, H., Liu, G.R., Bordas, S.P.A., Natarajan, S. and Rabczuk, T. (2013), "An adaptive singular ES-FEM for mechanics problems with singular field of arbitrary order", *Comput. Meth. Appl. Mech. Eng.*, **253**, 252-273. https://doi.org/10.1016/j.cma.2012.07.017.

Sukumar, N. and Tabarraei, A. (2004), "Conforming polygonal finite elements", *Int. J. Numer. Meth. Eng.*, **61**, 2045-2066. https://doi.org/10.1002/nme.1141.

Tabarraei, A. and Sukumar, N. (2006), "Application of polygonal finite elements in linear elasticity", *Int. J. Comput. Meth.*, **03**, 503-520. https://doi.org/10.1142/S021987620600117X.

Talischi, C., Paulino, G.H., Pereira, A. and Menezes, I.F.M. (2012), "PolyMesher: A general-purpose mesh generator for polygonal elements written in MATLAB", *Struct. Multidisc. Optim.*, **45**, 309-328. https://doi.org/10.1007/s00158-011-0706-z.

Talischi, C., Pereira, A., Paulino, G.H., Menezes, I.F.M. and Carvalho, M.S. (2014), "Polygonal finite elements for incompressible fluid flow", *Int. J. Numer. Meth. Fluid.*, **74**, 134-151. https://doi.org/10.1002/fld.3843.

Thomes, R.L. and Menandro, F.C.M. (2020), "Polygonal finite element: A comparison of the stiffness matrix integration methods". *Appl. Math. Comput.*, **375**, 125089. https://doi.org/10.1016/j.amc.2020.125089.

Timoshenko, S. and Goodier, J.N. (1970), *Theory of Elasticity*, 3rd Edition, McGraw-Hill, New York.

Wachspress, E.L. (1975), *A Rational Finite Element Basis*, Academic Press, New York.

Yan, D.M., Wang, W., Lévy, B. and Liu, Y. (2013), "Efficient computation of clipped Voronoi diagram for mesh generation", *Comput. Aid. Des.*, **45**, 843-852. https://doi.org/10.1016/j.cad.2011.09.004.
York.

CC

Appendix A. Calculation of natural coordinates in triangular domain

Here, we explain the method for calculating the natural coordinates corresponding to a specified position in a triangular domain. This calculation is required to obtain (r_1, s_1) and (r_2, s_2) in Eq. (13).

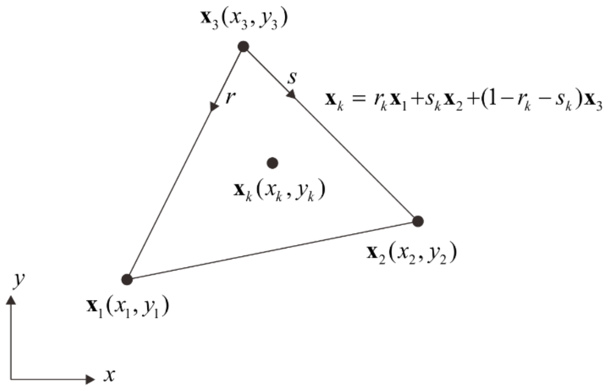

Fig. A1 Position vector of an arbitrary point $\boldsymbol{x}_k$ in the triangular domain

The position vector of a point $\mathbf{x}_k$ in the triangular domain shown in Fig. A1 can be expressed using the shape functions of the standard isoparametric procedure as follows

$$\mathbf{x}_k = r_k\mathbf{x}_1 + s_k\mathbf{x}_2 + (1 - r_k - s_k)\mathbf{x}_3 , \tag{26}$$

where $\mathbf{x}_1$, $\mathbf{x}_2$, and $\mathbf{x}_3$ are the position vectors of the vertices of the triangular domain; r_k and s_k are the natural coordinates of $\mathbf{x}_k$ to be determined.

The natural coordinates r_k and s_k are unknown values, and the positions of vertices $\mathbf{x}_i(x_i, y_i)$ and point $\mathbf{x}_k$ are specified. Eq. (26) can be expressed using the following matrix equation

$$\begin{bmatrix} x_1 - x_3 & x_2 - x_3 \\ y_1 - y_3 & y_2 - y_3 \end{bmatrix} \begin{bmatrix} r_k \\ s_k \end{bmatrix} = \begin{bmatrix} x_k - x_3 \\ y_k - y_3 \end{bmatrix}, \tag{27}$$

where (x_i, y_i) is the coordinates of $\mathbf{x}_i$ in the Cartesian coordinate system.

Finally, the natural coordinates r_k and s_k are calculated as follows

$$\begin{bmatrix} r_k \\ s_k \end{bmatrix} = \begin{bmatrix} x_1 - x_3 & x_2 - x_3 \\ y_1 - y_3 & y_2 - y_3 \end{bmatrix}^{-1} \begin{bmatrix} x_k - x_3 \\ y_k - y_3 \end{bmatrix}. \tag{28}$$

In general, natural coordinates in the triangular domain are defined between 0 and 1; however, if the position $\mathbf{x}_k$ is located outside the domain, the natural coordinates r_k and s_k can be negative values.